Structural Engineering and Mechanics, *Vol. 73, No. 2 (2020) 123-132*
DOI: https://doi.org/10.12989/sem.2020.73.2.123

Investigation of rotation and shear behaviours of complex steel spherical hinged bearings subject to axial tensile load

Kairong Shi[1,2a], Wenzhi Pan[1b], Zhengrong Jiang[*1,2] and Junfeng Lv[1c]

[1]*School of Civil Engineering and Transportation, South China University of Technology,*
[2]*State Key Laboratory of Subtropical Building Science, South China University of Technology,*
381 Wushan RD., Tianhe District, Guangzhou, P. R. China

(Received March 13, 2019, Revised September 8, 2019, Accepted September 23, 2019)

Abstract. Steel spherical hinged bearings have high loading capacity, reliable load transfer, flexible rotation with universal hinge and allowance of large displacement and rotation angle. However, bearings are in complex forced states subject to various load combinations, which lead to the significant influence on integral structural safety. Taking the large-tonnage complex steel spherical hinged bearings of Terminal 2 of Guangzhou Baiyun International Airport as an example, full-scale rotation and shear behaviour tests of the bearings subject to axial tensile load are carried out, and the corresponding finite element simulation analyses are conducted. The results of experiments and finite element simulations are in good agreement with the coincident development tendency of stress and deformation. In addition, the measured rotational moment is less than the calculated moment prescriptive by the code, and the relationship between horizontal displacement and horizontal shear force is linear. Finally, based on these results, the rotation and shear stiffness models of bearings subject to axial tensile load are proposed for the refinement analysis of integral structure.

Keywords: spherical bearings; mechanical properties; steel structure; finite element simulation; test

1. Introduction

Bearings are usually used to carry the vertical loads of an upper structure. As a result, their vertical loading capacity is one of their pivotal behaviour. However, for complex spatial structures, due to the particularity of the structural system and variety of loads, bearings are in complex and various forced states, including axial load, moment, shear load and their combinations (Wang *et al.* 2014, Shen *et al.* 2011).

Nowadays, the main types of bearings contain plate bearings, pot bearings, spherical bearings and rubber bearings (Shen *et al.* 2011, Dezfuli and Alam 2014, Ozkaya *et al.* 2011). Steel spherical bearings with high loading capacity, reliable load transfer, flexible rotation and allowance of large displacement and rotation angle, were developed from rubber pot bearings in the early 1970s. According to the displacement constraints in the horizontal direction, steel spherical bearings are divided into fixed bearings, uniaxial movement bearings and multiaxial movement bearings (Chinese National Standard 2009). After long-term development and research, bearings have been applied to large span spatial structures, high-rise buildings, bridge engineering, railway engineering and underground engineering (Karabork 2011, Yurdakul and Ates 2018, Chen *et al.* 2016).

Studies on spherical bearings and other types of bearings are focused on their structural and detailing design, mechanical analysis and experimental study. Han *et al.* (2014) conducted experimental and numerical studies on an innovative multi-spherical sliding friction isolation bearing. Concerning the decreased rotation flexibility of bearings subject to horizontal force, Shen *et al.* (2011) proposed a detailing improved method and conducted the corresponding computation and experiments. Han *et al.* (2011) carried out parametric and reliability analyses of the resistance of cast ball-and-socket support joints. Lee *et al.* (2014) proceed the experimental study on the compressive stress dependency of full scale low hardness lead rubber bearing. Iizuka (2000) proposed a macroscopic model for predicting the large-deformation behaviour of laminated rubber bearings by introducing finite deformation and nonlinear springs. Fan *et al.* (2015) carried out the optimum design of lead-rubber bearing system with uncertainty parameters under stochastic earthquake. Based on rheological models, Markou and Manolis (2016) introduced a series of novel 1D mechanical models for high damping rubber bearings.

The large-tonnage complex steel spherical hinged bearings are applied to Terminal 2 of Guangzhou Baiyun International Airport. The maximum design vertical tensile capacity of the bearings is 2000 kN. Subject to various load combinations, the bearings suffer from large axial compressive and tensile loads, horizontal loads and moments. Therefore, the bearings are in complex forced states, which affect the integral structural safety of the

*Corresponding author, Associate Professor
E-mail: zhrjiang@scut.edu.cn; 63287677@qq.com
[a] Ph.D., Associate Professor
[b] M.Sc. Student
c M.Sc. Student

ISSN: 1225-4568 (Print), 1598-6217 (Online)

Fig. 1 Architectural renderings of extension project of Guangzhou Baiyun International Airport

Fig. 2 Complex steel spherical hinged bearing

airport terminal.

Thus, full-scale test and finite element simulation analysis of the large-tonnage complex steel spherical hinged bearings are proposed in this study. The rotation and shear behaviours of the bearings subject to tensile load are studied as well. Finally, the new rotation and shear stiffness models of the bearings subject to axial tensile load are developed for the refinement analysis of integral structure of the airport terminal.

2. Engineering introduction and basic parameters of spherical bearings

Terminal 2 of Guangzhou Baiyun International Airport is a huge public transport building (Fig. 1). The largest elevation of single-layer grid structure of its steel roof is approximately 31 m. The largest span of the roof is 54 m, and its lengths are 598.3 m along the north–south direction and 304.4 m along the east–west direction. In addition, the total building area is approximately 150,000 m^2. Particularly, two types of steel spherical hinged bearings, namely, DBQJZ-GD-3000(2000)-5C and DBQJZ-GD-5000(1000)-2C, are arranged to support the steel roof.

Taking the spherical hinged bearing DBQJZ-GD-3000(2000)-5C (Fig. 2) as an example, its rotation and shear behaviours subject to axial tensile load are theoretically analysed and tested. The basic design parameters and components are listed in Tables 1 and 2. In addition, the cross-section drawing of the bearing is shown in Fig. 3.

Table 1 Basic parameters of the bearing

No.	Type	Value
1	Design vertical compressive capacity (kN)	3000
2	Design vertical tensile capacity (kN)	2000
3	Design horizontal capacity (kN)	2500
4	Allowable rotation angle (rad)	0.02
5	Diameter of the bearing (mm)	900
6	Height of the bearing (mm)	815
7	Elastic modulus of cast steel (MPa)	2.06×10^5
8	Density of cast steel (kg/m^3)	7850
9	Poisson ratio of cast steel	0.3

Table 2 Components of the bearing

No.	Component	Material
1	Composite slab of inner surface	SF-1
2	Top plate of stainless steel	1Cr18Ni9Ti
3	Main load-transfer component	G20Mn5
4	Anti-pluck component	Q345B
5	Spherical hinge component	Q345B
6	Base component	Q345B
7	Outer shell	G20Mn5QT
8	Sliding plate of anti-pluck component	PTFE
9	Sliding plate of load-transfer component	PTFE
10	Nut	G20Mn5QT
11	Sliding plate of spherical hinge component	PTFE
12	Sliding plate of base	PTFE
13	Temporary linked component	Q235B

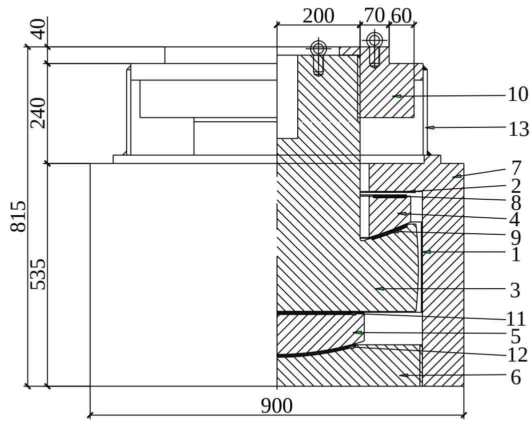

Fig. 3 Cross-section drawing of the bearing (the numbers indicate the components shown in Table 2)

3. Rotation behaviour of the bearing subject to axial tensile load

3.1 Finite element simulation analysis

To accurately predict the forced and deformation states of various components subject to certain load combinations, finite element analysis software ABAQUS is used for the refinement mechanical analysis.

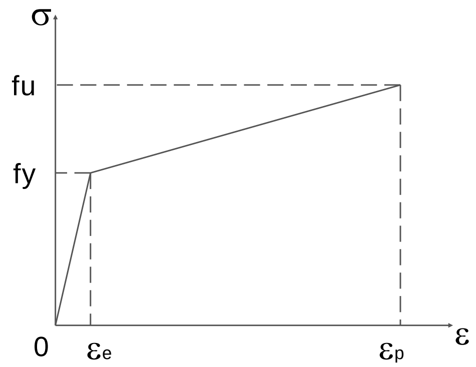

Fig. 4 Constitutive model of the materials

3.1.1 Finite element model

Model building and mesh generation

The geometrical model is built with mesh density between 20 mm and 25 mm (Fig. 3). The main components of the bearing are in sweep mesh form, whereas the upper and lower backing plates are in structured mesh form.

Material parameters

In accordance with Table 2, the density of steel is 7850 kg/m^3, and its elastic modulus is 2.06×10^5 MPa. For the G20Mn5 material, the yielding and ultimate strengths are 300 and 480 MPa, respectively, whereas for the G20Mn5QT material, they are 300 and 500 MPa, respectively. In addition, for the Q345B material, the yielding and ultimate strengths are 275 and 450 MPa, respectively. Taking the double-broken-line model as the constitutive model of the materials, the stiffness after yielding is reduced to 2% of the initial stiffness (Shi *et al*. 2011, Chung and Ip 2000, Epackachi *et al*. 2015), as shown in Fig. 4.

Contact setting

According to the structural characteristics and detailing of the spherical bearing, the contact pairs in the model contain the main load-transfer and spherical hinge components, main load-transfer and anti-pluck components, main load-transfer component and outer shell, anti-pluck component and outer shell, and spherical hinge and base components. The tangent friction coefficient is set as 0.03 (Chinese National Standard 2009). In addition, hard contact is set for normal contact, where the components are allowed to separate after contact.

Load and boundary conditions

In accordance with the actual rotation behaviour test procedure, a small initial displacement is added to ensure all the contact pairs are in contact states. The upper backing plate is set as the loading surface, whereas the lower backing plate is set as the hinged boundary surface, indicating that the displacements along the three axes are constrained. The entire top surface of the rigid loading slab is coupled to the center node of the surface, and the vertical concentrated force and the rotational moment are applied to the center node.

The finite element model is provided in Fig. 5.

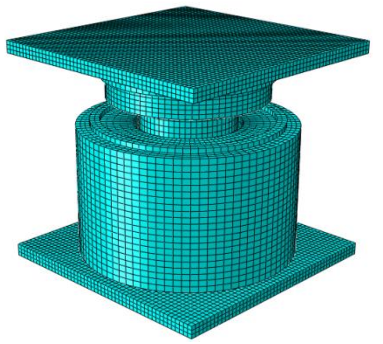

(a) 3D stereogram

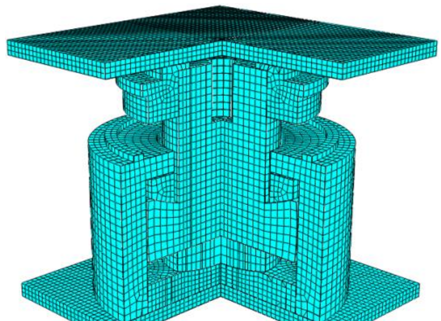

(b) Cross-section drawn

Fig. 5 Finite element model of the bearing

3.1.2 Finite element simulation result

Through the finite element calculation, the bearing state and deformation tendency of each loading phase can be obtained. With increasing rotational moment, the bearing state of the bearing subject to axial tensile load is given in Fig. 6.

After applying axial tensile load, high stress is induced at the top of the spherical bearing. The two contact pairs (anti-pluck component and outer shell, load-transfer and anti-pluck components) are in contact with high stress as well, as shown in Fig. 6(a). In Fig. 6(b), when rotational moment begins to be applied, no obvious rotation occurs due to static friction force. Then, with increasing rotational moment, static friction can be overcome, and obvious rotation occurs. In addition, the stress in the left part of the bearing increases, whereas that in the right decreases, as shown in Figs. 6(c) and 6(d). With the increasing application of moment, obvious horizontal displacement of anti-pluck and spherical hinge components occurs (Fig. 6(e)). Furthermore, high stress is induced in the left part of the bearing, especially for load-transfer and anti-pluck components.

3.2 Devices, steps and procedures of the test

3.2.1 Test devices

To obtain real test results, a full-scale test specimen is used. The axial tensile load is applied by two jacks on both sides of the bearing, whereas the rotational moment is induced by the difference between the two jacking forces. Hemispherical cushion block is placed between the jack and the loading arm (a steel beam with large flexural rigidity), which can ensure the loading direction of the jack is

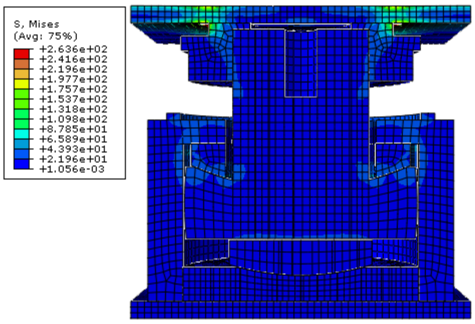

(a) State after applying 2000 kN axial tensile load without any rotational moment

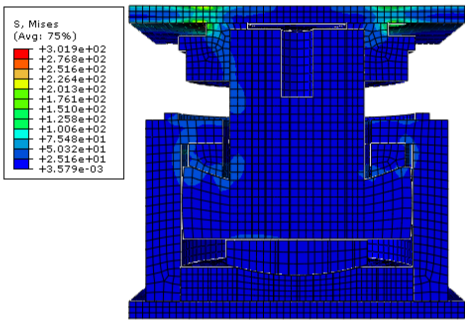

(b) State after applying 56 kN·m moment

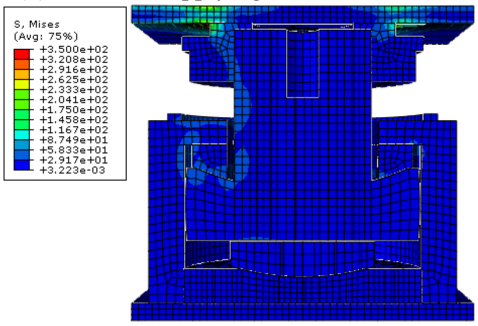

(c) State after applying 96 kN·m moment

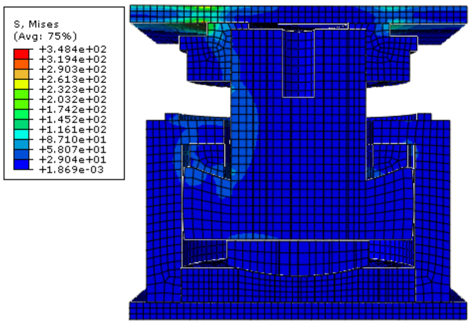

(d) State after applying 156 kN·m moment

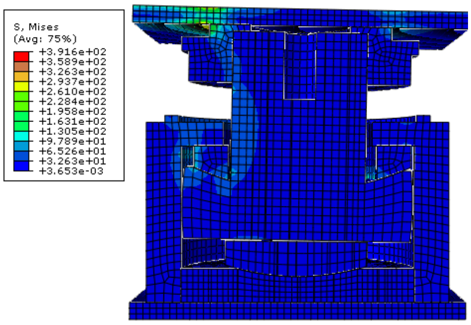

(e) State after applying 200 kN·m moment

Fig. 6 Rotational bearing state of spherical bearing during loading

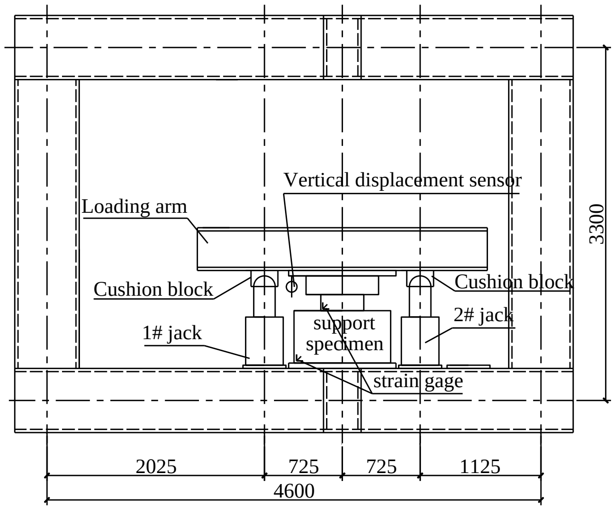

(a) Elevation of the test devices

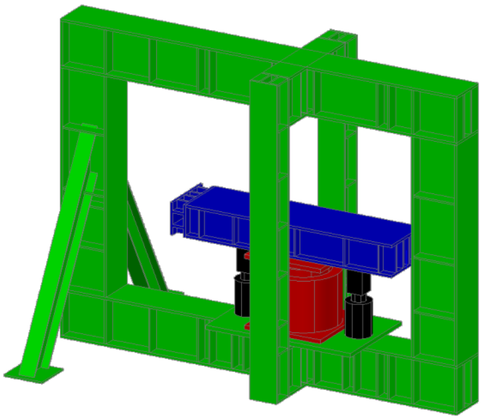

(b) 3D model of the test devices

(c) Actual arrangement of the test devices

Fig. 7 Test device for rotation behaviour testing of bearing subject to axial tensile load

always vertical. 3D models of the bearing, reaction frame for loading, loading arm and jacks are built to make the accurate arrangement of these devices before the test (Fig. 7).

3.2.2 Steps and procedures of the test

The maximum axial tensile load for the test is equal to the design vertical tensile capacity, which is 2000 kN. The detailed steps of the test are as follows:

(1) Test devices, measuring instruments and specimen are arranged according to Figs. 7 and 8. The two jacks (1# and 2# jacks) are used to apply the vertical tensile load through the loading arm, and the rotational moment is induced through the difference between the two jacking forces. To monitor the rotational state, the vertical displacement is measured by the displacement sensors placed at the four corners of the upper backing plate.

(2) For preloading, vertical tensile load is applied with constant loading speed from 0 kN to 2000 kN load. After retaining the 2000 kN tensile load for 3 minutes, unloading can be conducted, and the interval for preloading is set to 3 minutes. The abovementioned preloading is repeated three times.

(3) For formal loading, vertical tensile load is applied with constant loading speed from 0 kN to 2000 kN load as well. After retaining the 2000 kN tensile load for 3 minutes, testing data are recorded.

(4) For applying the rotational moment, the jacking force of 1# jack gradually increases, whereas that of 2# jack synchronously decreases. Throughout the process, the total jacking force of 1# and 2# jacks remains constant and equal to the design vertical tensile capacity. When there are obvious changes of the displacement sensors, it can be inferred that certain rotation of the bearing has occurred. In addition, the jacking forces and the readings of the displacement sensors and strain gages are recorded. The abovementioned formal loading is conducted three times.

(5) The measured rotational moment is expressed as follows:

$$M_\theta = P_1 \cdot l_1 - P_2 \cdot l_2 \tag{1}$$

Where P_1, P_2 are the jacking forces of 1# and 2# jacks, respectively, and l_1, l_2 are the distance from the loading point of 1# and 2# jacks to the center of the bearing, respectively.

3.3 Comparison of test data and finite element simulation results

3.3.1 Rotation capacity

Combining the vertical displacements of key points from the test data and simulation results, the relation curves between rotational moment and angle for rotation behaviour test of bearing subject to axial tensile load can be plotted, as given in Fig. 9.

As shown in Fig. 9, at the beginning, slight rotation occurs in the bearing. Then, when the average rotational moment increases to approximately 40 kN·m, obvious rotation occurs. Furthermore, after reaching 170 kN·m, significant rotation occurs. According to the code (Chinese National Standard 2009), the calculated rotational moment of the bearing is as follows:

$$M_\theta = R_{ck} \cdot \mu_f \cdot R = 2000 \times 0.03 \times 0.7778 = 47kN \cdot m \tag{2}$$

where R_{ck} is the design vertical capacity, μ_f is the design friction coefficient, and R is the spherical radius. Evidently, the measured rotational moment (40 kN·m) is less than the calculated moment (47 kN·m), which satisfies the requirements.

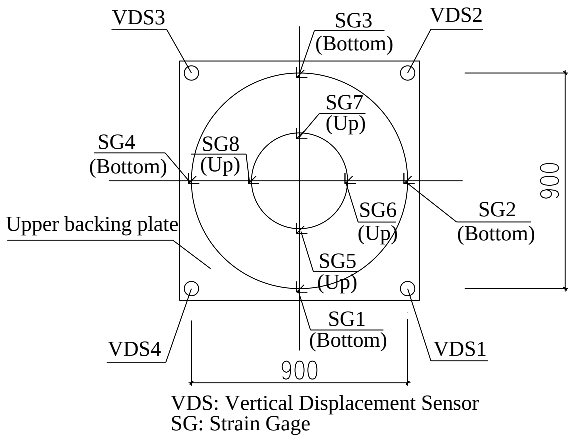

Fig. 8 Arrangement of measuring points for rotation behaviour test of bearing subject to axial tensile load (the elevation of measuring points can be referred to Fig. 7(a))

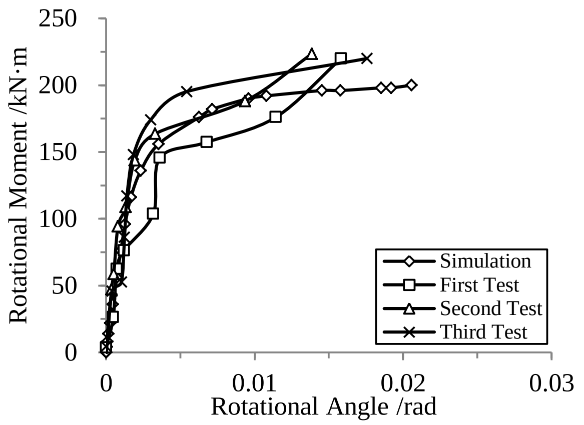

Fig. 9 Relation curves between rotational moment and angle

The comparison of the four curves indicated that the test data and simulation results are in good agreement with the same development tendency.

3.3.2 Stress

During the loading process, the test bearing is in complex 3D stress states. The strain values of measuring points are transformed into von Mises equivalent stress and compared with the simulation results. The key measuring points of the outer shell and load-transfer component are selected for comparison, as provided in Fig. 10.

Fig. 10(a) shows that the development tendencies of the four curves are consistent and increasing throughout the process, which indicates that the experimental and simulation results agree well. Fig. 10(b) shows that, with increasing rotational moment, the stress of measuring point 8 also increases. The simulation results can accurately reflect the actual rotation behaviour of the bearing. Combining the stress state of the eight key points in Fig. 8, the maximum stress value of all the points along the entire process is approximately 65 MPa, which is much less than the yielding strength of steel. Throughout the test, no destructions of the bearing were observed.

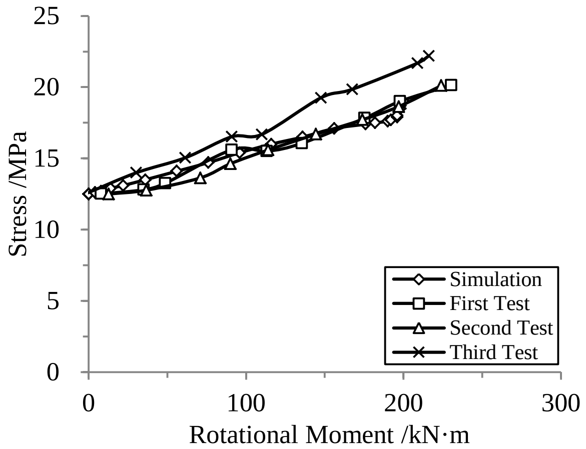

(a) Measuring point 4 of outer shell

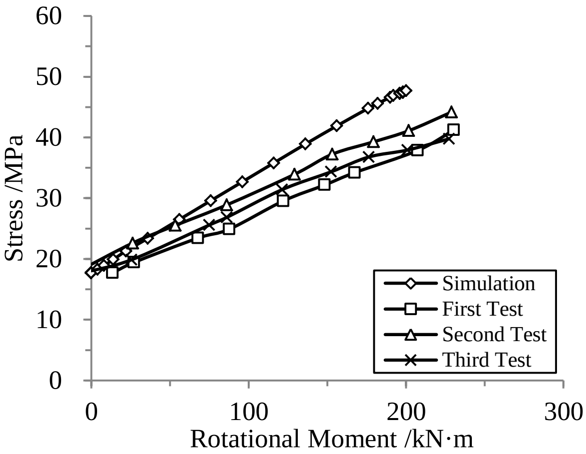

(b) Measuring point 8 of load-transfer component

Fig. 10 Stress comparisons of key measuring points

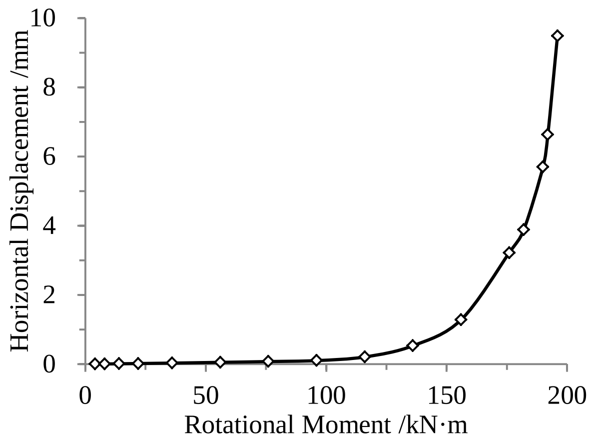

Fig. 11 Horizontal displacement curve of anti-pluck component

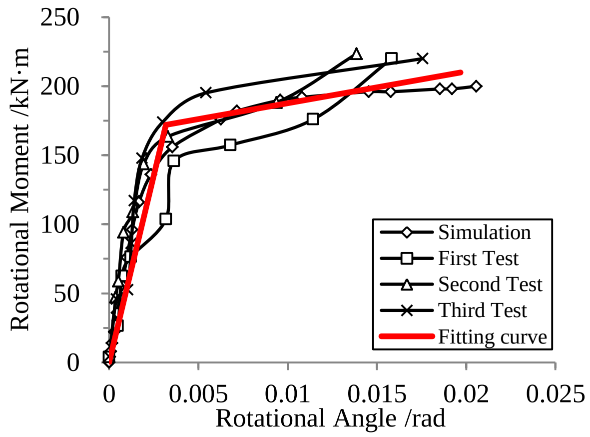

Fig. 12 Fitting curve of relation between rotational moment and angle

3.4 Rotation stiffness model of bearing subject to axial tensile load

According to the relation curves between rotational moment and angle in Fig. 9, at the beginning, slight rotation of the bearing occurs, which corresponds to a large slope of the relation curve. When the rotational moment exceeds approximately 170 kN·m, significant rotation of the bearing occurs, corresponding to a relatively small slope of the curve. Considering the finite element simulation results in Fig. 6(d), the slope decreases because of the large horizontal displacement of anti-pluck component. As shown in Fig. 11, after reaching approximately 170 kN·m rotational moment, the horizontal displacement increases rapidly, leading to non-negligible eccentric application of vertical tensile load. Due to the eccentric effect and increasing rotational moment, significant rotation occurs, leading to the decrease of the slope. Thus, the relation curve between rotational moment and angle can be simplified as a double-broken-line model, and the inflection point is located at approximately 170 kN·m. Combining the test data and simulation results, the fitting curve is formed by the least square method, as given in Fig. 12.

Fig. 12 shows that the fitting curve, test curves and simulation curve are coincident. The initial rotation stiffness is 54300 kN·m/rad, whereas the reduced rotation stiffness is 2300 kN·m/rad, which is only 4.2% of the initial stiffness. Furthermore, the inflection point is located at the point (172 kN·m, 0.00317 rad). Thus, the equation of rotation stiffness model can be expressed as follows:

$$M = \begin{cases} 54300\theta, & 0 \le \theta \le 0.00317 rad \\ 165 + 2300\theta, & \theta > 0.00317 rad \end{cases} \tag{3}$$

where M is the rotational moment with the unit of kN·m and θ is the rotational angle with the unit of rad.

The proposed rotation stiffness model of the bearings subject to axial tensile load can be used for the refinement analysis of integral structure of the airport terminal.

4. Shear behaviour of bearing subject to axial tensile load

4.1 Finite element simulation analysis

The geometric parameters, material parameters, contact setting and boundary conditions of shear behaviour model are the same as in Section 3.1.1. According to the actual shear behaviour test procedure, the bearing state and deformation tendency of each loading phase can be obtained through finite element calculation. With the

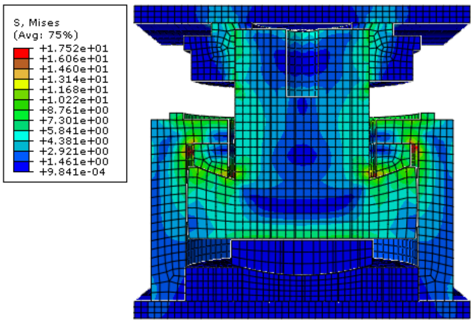

(a) State after applying 1200 kN axial tensile load without any shear force

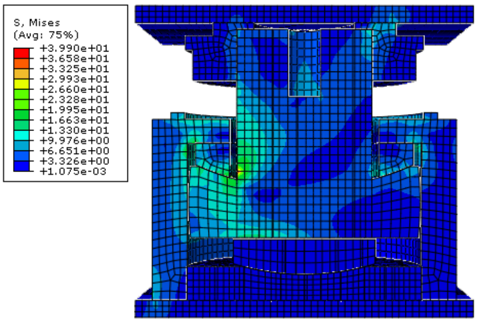

(b) State after applying 300 kN shear force

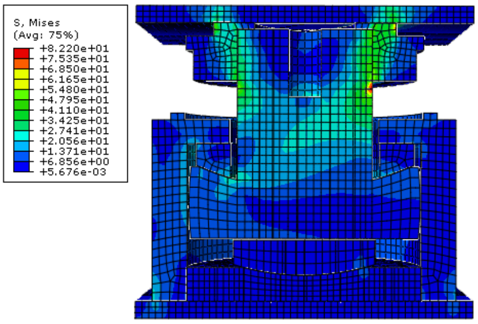

(c) State after applying 1500 kN shear force

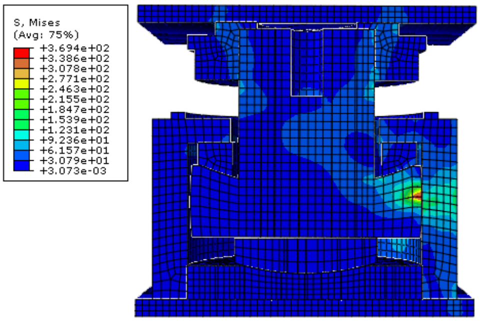

(d) State after applying 2700 kN shear force

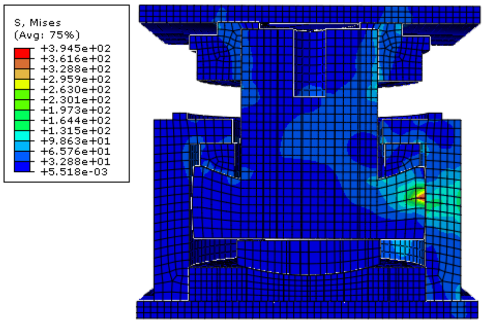

(e) State after applying 3000 kN shear force

Fig. 13 Shear bearing state of spherical bearing during loading

increasing shear force, the state of the bearing subject to axial tensile load is provided in Fig. 13.

Fig. 13(a) shows that after applying axial tensile load, the maximum stress induced in the bearing is approximately 17.52 MPa, which is much smaller than its steel yielding strength. Due to the moment caused by shear force, when shear force begins to be applied, the stress of the left part increases, whereas that of the right part decreases, as given in Fig. 13(b). As shown in Fig. 13(c), with increasing shear force, obvious horizontal displacement of anti-pluck component occurs, which leads to stress redistribution of the bearing. Furthermore, due to the large shear force, significant horizontal displacement of load-transfer component occurs, leading to the contact between load-transfer component and outer shell. The maximum stress is located at the contact point, as provided in Figs. 6(d) and (e).

4.2 Devices, steps and procedures of the test

4.2.1 Test devices

Similar to rotation behaviour test, the full-scale specimen is also used in shear behaviour test. The axial tensile load is applied by two jacks on both sides of the bearing, whereas the shear force is applied by the jack arranged horizontally. Roller slider is placed between the jack and the loading arm, which can ensure the accuracy of horizontally loading (shear force). During the horizontally loading process, the total jacking force applied by 1# and 2# jack remains constant. 3D models of the test devices are built to make the accurate arrangement before the test (Fig. 14).

4.2.2 Steps and procedures of the test

The maximum axial tensile load for test is equal to 120% of the design vertical tensile capacity, which is 2400 kN. The maximum shear force for the test is equal to 120% of the design horizontal capacity, which is 3000 kN. The detailed steps of the test are as follows:

(1) Test devices, measuring instruments and specimen are arranged according to Figs. 14 and 15. The 1# and 2# jacks are used to apply the vertical tensile load through the loading arm, whereas the 3# jack is used to apply the shear force. The vertical and horizontal displacements and strains are measured by the displacement sensors and strain gages.

(2) For preloading, vertical tensile load is applied by 1# and 2# jacks with constant loading speed from 0 to half of the maximum axial tensile load (1200 kN). Then, the shear force is applied by 3# jack from 0% to 20% of the maximum shear force for test (500 kN). After retaining the prescriptive loads for 3 minutes, unloading can be conducted, and the interval for preloading is set to 3 minutes. The abovementioned preloading is repeated three times.

(3) For formal loading, the shear force for test is uniformly divided into 10 grades. At the beginning, 1200 kN vertical tensile load is applied by 1# and 2# jacks, and 15 kN shear force is applied as the initial horizontal force by 3# jack. For each grade, after retaining the prescriptive load for 2 minutes, the jacking forces and the readings of the displacement sensors and strain gages are recorded.

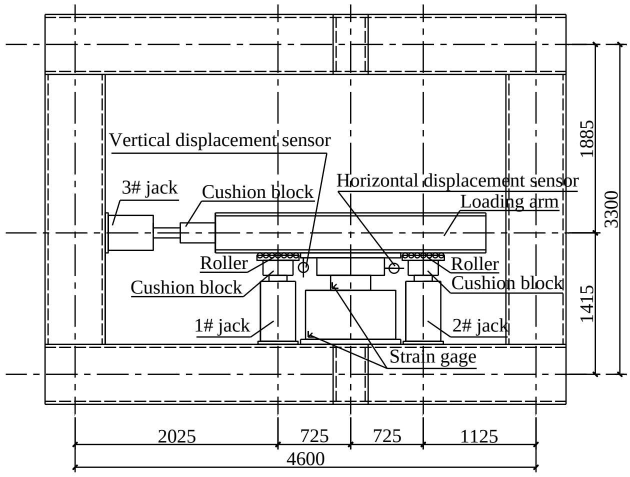

(a) Elevation of the test devices

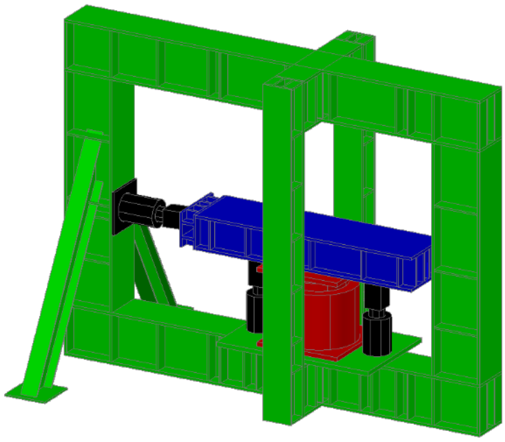

(b) 3D model of the test devices

(c) Actual arrangement of the test devices

Fig. 14 Test device for shear behaviour test of bearing subject to axial tensile load

After the force applied by 3# jack reaches 90% of the maximum shear force for test (2700 kN), 2400 kN axial tensile load and 3000 kN shear force are applied to the bearing as the last loading grade. After 3 minutes for static loading, unloading can be carried out. The abovementioned formal loading is conducted three times.

4.3 Comparison of test data and finite element simulation results

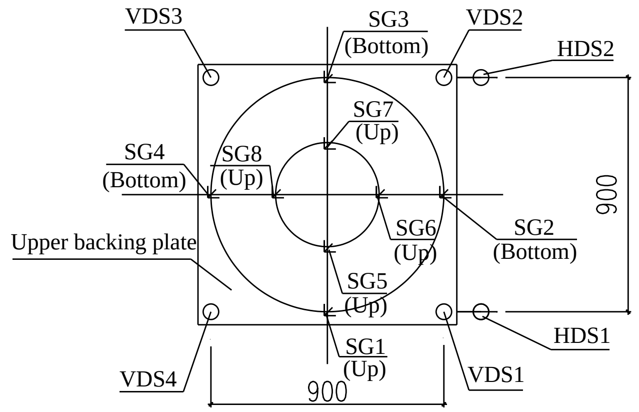

VDS: Vertical Displacement Sensor
HDS: Horizontal Displacement Sensor
SG: Strain Gage

Fig. 15 Arrangement of measuring points for shear behaviour test of bearing subject to axial tensile load (the elevation of measuring points can be referred to Fig. 14(a))

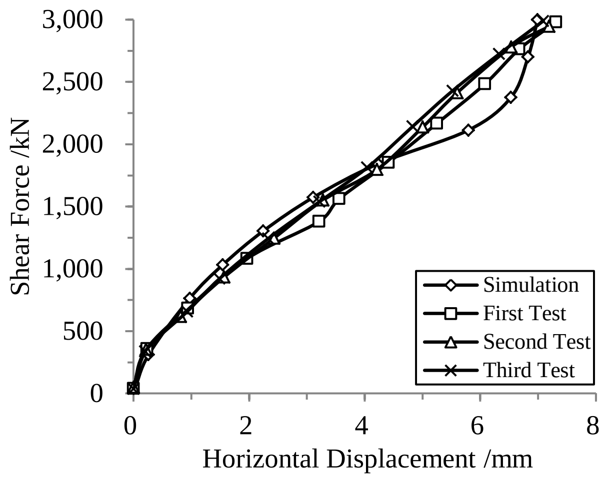

Fig. 16 Relation curves between shear force and horizontal displacement

4.3.1 Horizontal displacement

Combining the horizontal displacement of key points from the test data and simulation results, the relation curves between shear force and horizontal displacement for shear behaviour test of bearing subject to axial tensile load can be plotted (Fig. 16).

As shown in Fig. 16, the horizontal displacement increases with increasing shear force. It is indicated that the relationship between horizontal displacement and horizontal shear force is linear, which satisfies the code's requirements. The comparison of the four curves revealed that the test data and simulation results are in good agreement with the same development tendency.

4.3.2 Stress

The strain values of measuring points are transformed into von Mises equivalent stress and compared with simulation results. Then, the key measuring points of the outer shell and load-transfer component are selected for comparison, as shown in Fig. 17.

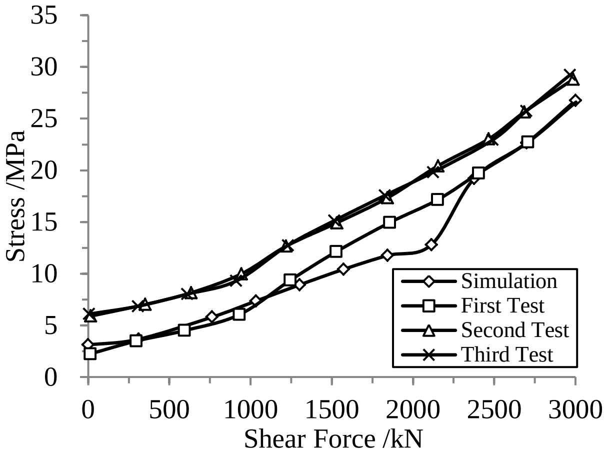

(a) Measuring point 3 of outer shell

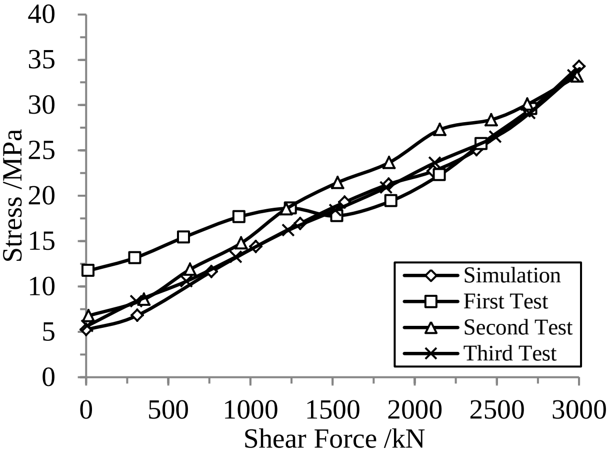

(b) Measuring point 5 of load-transfer component

Fig. 17 Stress comparisons of key measuring points

Fig. 17(a) shows that the development tendencies of the four curves are consistent and increasing throughout the process, which indicates that the experimental and simulation results agree well. As for Fig. 17(b), with increasing shear force, the stress of measuring point 5 also increases. The simulation results can accurately reflect the actual shear behaviours of the bearing. Combining the stress state of the eight key points in Fig. 15, the maximum stress value of all the points along the entire process is approximately 67 MPa, which is much less than the yielding strength of steel. Throughout the test, no destructions of the bearing were observed.

4.4 Shear stiffness model of bearing subject to axial tensile load

According to the relation curves between shear force and horizontal displacement in Fig. 16, the four curves can be simplified into straight lines. Then, the linear model can be used for fitting relation curve between shear force and horizontal displacement. Combining the test data and simulation results, the fitting curve is formed by the least square method, as shown in Fig. 18.

In accordance with Fig. 18, the fitting curve, test curves and simulation curve are coincident. The shear stiffness is

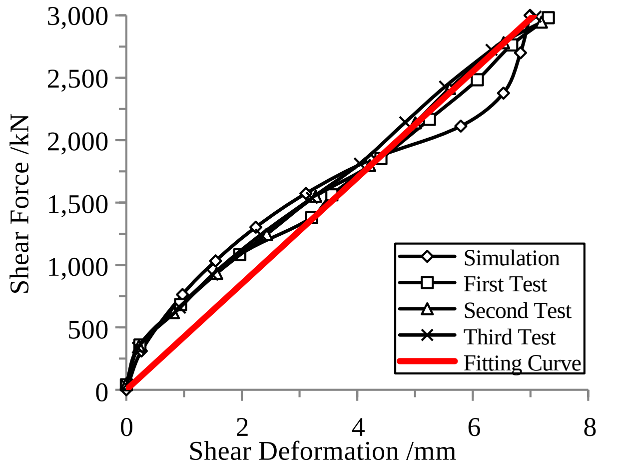

Fig. 18 Fitting curve of relation between shear force and shear deformation

simplified as 425 kN/mm. Thus, the equation of shear stiffness model can be expressed as follows:

$$F = 425d \tag{4}$$

where F is the shear force with the unit of kN and d is the horizontal displacement with the unit of mm.

The proposed shear stiffness model of the bearings subject to axial tensile load can be used for the refinement analysis of integral structure of the airport terminal.

5. Conclusions

Taking the large-tonnage complex steel spherical hinged bearings of Terminal 2 of Guangzhou Baiyun International Airport as an example, full-scale rotation and shear behaviour tests of the bearing subject to axial tensile load are carried out, and the corresponding finite element simulation analyses are conducted. Some research conclusions can be drawn as follows:

- The test data and simulation results are in good agreement with the same development tendencies of stress and deformation. The stress values of all the measuring points along the entire process are much lesser than the yielding strength of steel. Furthermore, the bearing is in safe state and satisfies the design requirements.
- The measured rotational moment is less than the calculated moment, which satisfies the requirements. In addition, the horizontal displacement increases with the increasing shear force. It is indicated that the relationship between shear displacement and shear force is linear, which also satisfies the requirements.
- The presented fitting curves, test curves and finite element simulation curves are coincident. Therefore, in engineering application, the mechanical properties of the bearing can be accurately described according to the proposed stiffness models.
- Based on the results, the double-folded rotational stiffness model and linear shear stiffness model of the bearing subject to axial tensile load can be used for the refinement analysis of integral structure.

Acknowledgments

This research was financially supported by the Opening Project of State Key Laboratory of Subtropical Building Science, South China University of Technology, China (grant number 2019ZB27) and the Science and Technology Program of Guangzhou, China (grant number 1563000257).

References

Chen, Z.Y., Zhao, H. and Lou, M.L. (2016), "Seismic performance and optimal design of framed underground structures with lead-rubber bearings", *Struct. Eng. Mech.,* **58**(2), 259-276. https://doi.org/10.12989/sem.2016.58.2.259.

Chinese Nation Standards (2009), Spherical bearings for bridges (GB/T 17955-2009), Standardization Administration of China, Beijing, China. (in Chinese)

Chung, K.F. and Ip, K.H. (2000), "Finite element modeling of bolted connections between cold-formed steel strips and hot rolled steel plates under static shear loading", *Eng. Struct.*, **22**(10), 1271-1284. https://doi.org/10.1016/S0141-0296(99)00082-6.

Dezfuli F.H. and Alam M.S. (2014), "Performance-based assessment and design of FRP-based high damping rubber bearing incorporated with shape memory alloy wires", *Eng. Struct.*, **61**(61), 166-183. https://doi.org/10.1016/j.engstruct.2014.01.008.

Epackachi, S., Whittaker, A.S., Varma, A.H. and Kurt, E.G. (2015), "Finite element modeling of steel-plate concrete composite wall piers", *Eng. Struct.*, **100**, 369-384. https://doi.org/10.1016/j.engstruct.2015.06.023

Fan, J., Long, X.H. and Zhang, Y.P. (2015), "Optimum design of lead-rubber bearing system with uncertainty parameters", *Struct. Eng. Mech.*, **56**(6), 959-982. https://doi.org/10.12989/sem.2015.56.6.959.

Han, Q., Wen, J., Lin, L. and Jia, J. 2014), "Experimental and numerical studies on multi-spherical sliding friction isolation bearing", *J. Vibroengineering*, **16**(5), 2394-2405.

Han, Q.H., Lu, Y. and Jin, M.C. (2011), "Resistance partial factor and reliability of cast ball-and-socket support joint", *Trans. Tianjin Univ.*, **17**(6), 391-396. https://doi.org/10.1007/s12209-011-1617-1.

Iizuka, M. (2000), "A macroscopic model for predicting large-deformation behaviors of laminated rubber bearings", *Eng. Struct.*, **22**(4), 323-334. https://doi.org/10.1016/S0141-0296(98)00118-7.

Karabork, T. (2011), "Performance of multi-storey structures with high damping rubber bearing base isolation systems", *Struct. Eng. Mech.*, **39**(39), 399-410. https://doi.org/10.12989/sem.2011.39.3.399.

Lee, H., Cho, M., Kim, S., Park, J. and Jang, K. (2014), "Experimental study on the compressive stress dependency of full scale low hardness lead rubber bearing", *Struct. Eng. Mech.*, **50**(1), 89-103. https://doi.org/10.12989/sem.2014.50.1.089.

Markou, A.A. and Manolis, G.D. (2016), "Mechanical models for shear behavior in high damping rubber bearings", *Soil Dyn. Earthq. Eng.*, **90**, 221-226. https://doi.org/10.1016/j.soildyn.2016.08.035.

Ozkaya, C., Akyuz, U., Caner, A., Dicleli, M. U. R. A. T., & Pınarbası, S. (2011), "Development of a new rubber seismic isolator: 'Ball Rubber Bearing (BRB)'", *Earthq. Eng. Struct. Dyn.*, **40**(12), 1337-1352. https://doi.org/10.1002/eqe.1091.

Shen, Y.L., Fan, Z. and Zhang P.J. (2011), "Analysis of design for spherical bearings in building structures", *Steel Struct.*, **26**(6), 6-11.

Shi, Y.J., Wang, M. and Wang, Y.Q. (2011), "Experimental and constitutive model study of structural steel under cyclic loading", *J. Constr. Steel Res.*, **67**(8), 1185-1197. https://doi.org/10.1016/j.jcsr.2011.02.011.

Wang, R.Z., Chen, S.K., Liu, K.Y., Wang, C., Chang, K.C. and Chen, S.H. (2014), "Analytical simulations of the steel-laminated elastomeric bridge bearing", *J. Mech.*, **30**(4), 373-382.

Yurdakul, M. and Ates, S. (2018), "Stochastic responses of isolated bridge with triple concave friction pendulum bearing under spatially varying ground motion", *Struct. Eng. Mech.*, **65**(6), 771-784. https://doi.org/10.12989/sem.2018.65.6.771.

CC